Targeted Nanofitin-drug Conjugates Achieve Efficient Tumor Delivery and Therapeutic Effect in an EGFR^{pos} Mouse Xenograft Model

Simon Huet[1], Magali Zeisser Labouebe[2,3], Rute Castro[4], Perrine Jacquot[1], Jessy Pedrault[1], Sébastien Viollet[1], Gaetan Van Simaeys[5], Gilles Doumont[5], Lionel Larbanoix[6], Egor Zindy[5], António E. Cunha[4], Leonardo Scapozza[2,3], and Mathieu Cinier[1]

ABSTRACT

Adjusting the molecular size, the valency and the pharmacokinetics of drug conjugates are as many leverages to improve their therapeutic window, notably by affecting tumor penetration, renal clearance, and short systemic exposure. In that regard, small tumor-targeting ligands are gaining attention. In this study, we demonstrate the benefits of the small Nanofitin alternative scaffolds (7 kDa) as selective tumor-targeting modules for the generation of drug conjugates, focusing on Nanofitins B10 and D8 directed against the EGFR. Owing to their small size and monovalent format, the two Nanofitins displayed a fast and deep tumor penetration in EGFR-positive A431 xenografts in BALB/c nude mice after intravenous administration, yielding to a targeting of respectively 67.9% ± 14.1 and 98.9% ± 0.7 of the tumor cells as demonstrated by IHC. Conjugation with the monomethyl auristatin E toxin provided homogeneous Nanofitin-drug conjugates, with an overall yield of ≥97%, for *in vivo* assessment in a curative xenograft model using bioluminescent, EGFR-positive, A431 cells in BALB/c nude mice. Internalization was found critical for efficient release of the toxin. Hence, the intravenous administration of the D8-based construct showed significant antitumor effect *in vivo* as determined by monitoring tumor volumes and bioluminescence levels over 2 months.

Introduction

The treatment of solid tumors with pharmacologic modalities remains challenging, notably because their antigenic heterogeneity (1) and limited permeability to macromolecules (2) can lead to a suboptimal drug exposure. Although chemotherapeutics benefit from the advantage of a broad diffusion within the tumor tissue, their lack of specificity is limiting their therapeutic window (3, 4). Their mechanism of action is mostly restricted to the killing of dividing cells, which hampers their effect on dormant and slow-dividing cancer cells (5). Antibody-based immunotherapies have the potential to preferentially target the tumor cells but display a slow diffusion in tumors (6), leaving some of the deepest tumor cells unexposed to the drug. Limited diffusion of antibodies is attributed to distinct factors (7). First, their high molecular weight hinders their passive diffusion from the blood vessel even if facilitated by the well-known Enhanced Permeability and Retention (EPR) effect. Second, the diffusion of the antibody within the tumor tissue can be restricted by the so-called barrier site effect (8), referring to the trapping of the antibody in the surrounding of the vasculature. Moreover, the cytotoxic activity of antibody-based therapeutics often relies on antibody-dependent cell cytotoxicity (ADCC), which can be crippled in the context of an immunosuppressive tumor microenvironment (9). To restore cytotoxic activity, combining chemo- and immunotherapies is now the standard of care for many cancer diseases.

Since the approval of Kadcyla in 2013, antibody–drug conjugates (ADC) have been used to combine the well-established nature and selectivity of antibody therapeutics with the high cytotoxic potency of small molecule toxins. Despite showing promise and undergoing continuous improvements as a disruptive technology in oncology (10), the use of ADCs for treating solid tumors remains limited by inherent constraints of antibodies. In addition to their poor extravasation (11), ADCs display antibody-like pharmacokinetic profiles with a prolonged plasma half-life that can foster off-target release of the toxin and subsequent toxicity (12, 13). Besides, antibodies undergo a systemic clearance mainly driven by hepatic metabolism (14), leading to hepatic and gastrointestinal toxicities in the case of an ADC that can limit its therapeutic window. Finally, the tripartite assembly of the ADC (antibody-linker-cytotoxic payload) requires a demanding process that can result in ADCs of lower solubility and homogeneity than their parent antibodies and the generation of immunogenic aggregates (15).

Next-generation drug conjugate therapies would benefit from a better control of their homogeneity, biodistribution and cell engagement (16). An alternative strategy consists in replacing the antibody with a ligand of less than 10 kDa (17–20) allowing faster accumulation and broader diffusion within the tumor together with a lesser systemic exposure compared with conventional antibodies (21, 22). As a support to this rationale, robust preclinical efficiency has been demonstrated with the bicycle peptide-toxin conjugates BT1718 and BT5528 (23) currently evaluated in clinical trials against solid tumors (24, 25).

[1]Affilogic SAS, Nantes, France. [2]Pharmaceutical Biochemistry Group, School of Pharmaceutical Sciences, University of Geneva, Geneva, Switzerland. [3]Institute of Pharmaceutical Sciences of Western Switzerland, University of Geneva, Geneva, Switzerland. [4]iBET, Instituto de Biologia Experimental e Tecnológica, Oeiras, Portugal. [5]CMMI, Center for Microscopy and Molecular Imaging, Université libre de Bruxelles, Charleroi (Gosselies), Belgium. [6]CMMI, Center for Microscopy and Molecular Imaging, Université de Mons, Charleroi (Gosselies), Belgium.

Corresponding Author: Simon Huet, AFFILOGIC, 24 rue de la Rainière, 44300 Nantes, France. E-mail: simon@affilogic.com

Mol Cancer Ther 2023;22:1343–51

doi: 10.1158/1535-7163.MCT-22-0805

In this publication, we describe the use of Nanofitins for the engineering of drug conjugates, as they benefit from the desired properties of non-antibody alternative scaffolds (26): small, single-chain, cysteine-free, and without posttranslational modification. Nanofitins can be engineered to bind with high affinity and specificity to a wide variety of biologically relevant targets (27–34). They are amenable to regioselective enzymatic or chemical conjugation by the introduction of a unique acceptor sequence (sortase-tag, cysteine. . .) using straightforward molecular approaches, while preserving the original pharmacologic and stability properties of the parent protein. Their extreme resistance to temperature (Tm > 70°C), pH (1–13) and their ability to spontaneously fold in aqueous solutions make them naturally compatible with a broad range of conjugation reaction conditions, as well as with synthetic manufacturing.

In a previous study, we demonstrated with a radiolabeled, non-internalizing, Nanofitin targeting the EGFR that high tumor-to-blood contrast can be achieved as fast as 90 minutes postinjection (32), thanks to its fast tumor uptake and rapid elimination from the bloodstream. Clearance was mainly mediated by renal excretion, which is a promising feature to avoid hepatic toxicity. Here, we describe the development of a Nanofitin-drug conjugate on the basis of an internalizing antiEGFR Nanofitin. We illustrate the superior diffusion rate of antiEGFR Nanofitins in commonly used A431-derived solid tumors, in comparison with the therapeutic antibody Cetuximab. Finally, we demonstrate the regioselective conjugation to the combination of Monomethyl auristatin E and valine-citrulline linker (vc-MMAE) moieties, widely used for ADCs (10), and the ability of the resulting D8-vc-MMAE conjugate to promote a significant antitumor activity *in vivo*.

Materials and Methods

Production and purification of tag-free Nanofitins

E. coli DH5α clones expressing tag-free Nanofitins D8, B10 and irrNF (irrelevant Nanofitin), bearing a C-terminal cysteine (Supplementary Fig. S1), were cultivated in M9 minimal medium, in shake-flasks (37°C, 180 rpm). Nanofitin expression was induced with IPTG (1 mmol/L) for 4 hours (D8) or 16 hours (B10 and irrNF). Cells were harvested by centrifugation using a Beckman Avanti J-HC. Biomass was disrupted in APV 2000 homogenizer, and cell debris removed by centrifugation (30 minutes, 31000*g*, 4°C). Supernatants were clarified by filtration through a 0.2 μm filter. Filtrates were treated by tangential flow ultrafiltration (TFF) with 30 and 5 kDa MWCO membranes (Sartorius): after purification (30 kDa MWCO), samples were concentrated and diafiltrated (5 kDa MWCO). Each Nanofitin was purified by cation exchange chromatography using Fractogel SO3-resin (Merck EMD). Nanofitins D8 and B10 were polished by size exclusion chromatography using a Superdex 75 column (Cytiva). Purified Nanofitins were formulated in 20 mmol/L HEPES containing 150 mmol/L of NaCl, pH 7.4, concentrated by TFF (5 kDa MWCO) and loaded onto a Sartobind STIC nano column (Sartorius) for endotoxin removal. Protein purity was addressed using standard SDS-PAGE analysis and mass spectrometry (MS). Endotoxin levels were assessed using the Endosafe-PTS LAL analysis (Charles River).

Binding affinity determination by biolayer interferometry

Binding kinetic parameters of the antiEGFR Nanofitins B10 and D8 drug conjugates, B10-vc-MMAE and D8-vc-MMAE, were measured by interferometry (Octet RED96, ForteBio, RRID:SCR_023267). Recombinant Human EGFR Fc chimera protein (344-ER, R&D Systems) was diluted to 5 μg/mL and loaded on protein A biosensors at 1 nm before equilibration for 60 seconds. Binding kinetics were then evaluated by simultaneously exposing biosensors to various concentrations (500, 125, 31.25, 7.81, and 0 nmol/L) of B10-vc-MMAE or D8-vc-MMAE. Association and dissociation steps were measured for 3 minutes each. Unless otherwise specified, all steps were performed in TBS containing 0.002% Tween 20 and 0.01% BSA. Biosensors were regenerated using three cycles of alternating washes for 10 seconds in Glycine 10 mmol/L pH 2.5 and in TBS. All the steps were run at 30°C and 1,000 rpm. The biosensor exposed to the 0 nmol/L concentration was used as a background reference. Sensorgrams were processed using a single reference subtraction and analyzed using the Octet Data Analysis software (ForteBio). Fitting was performed with a 1:1 binding fit model and illustrated with GraphPad Prism 6 (GraphPad Inc, RRID: SCR_002798).

Affinities were also determined for cysteine-free and HA-tagged (35) Nanofitins (500, 250, 125, 62.5, 31.25, 15.63, 7.81, and 0 nmol/L), either on human EGFR as described above, or on murine EGFR by using Recombinant Mouse EGFR Fc chimera protein (1280-ER, R&D Systems) for the loading step.

Nanofitin-drug conjugation

Conjugation

Nanofitins bearing a C-terminal cysteine were treated by 10 mg batches (2 mg/mL) overnight at 4°C with TCEP (4× molar excess from stock solution at 1 mol/L). Five molar equivalents of mc-vc-PAB-MonoMethyl Auristatin E (vc-MMAE, Ontario Chemicals) were added to the reduced Nanofitins from the stock solution of vc-MMAE at 10 mg/mL in DMSO and left under agitation under argon (2 hours, 25°C). The excess of unconjugated vc-MMAE was removed on a spin PD-10 column (Sephadex G-25, GE Healthcare) before purification of the NF conjugates by size exclusion chromatography on a HiLoad 16/60 Superdex 75 PG column (GE Healthcare) with HEPES buffer at 1.2 mL/min. Fractions containing the Nanofitin-vc-MMAE conjugates were pooled and concentrated to about 5 mg/mL using Pierce protein concentrators 3K. The final product was characterized by UPLC-RP/MS. The Nanofitin-vc-MMAE conjugates were sterile-filtered and stored at −80°C for further use.

MS

Product identity (Supplementary Fig. S1) was confirmed by injection of 5 μL on an Acquity UPLC system coupled to a XEVO TQ-MS detector (Waters). Separation was performed at 60°C using an Acquity UPLC BEHC18 column (150 × 2.1 mm I.D., 1.7 μmol/L) at a flow rate of 0.5 mL/minute with a gradient mode over 8 minutes. The mobile phase consisted of a mixture of water with 0.1% v/v formic acid (A) and acetonitrile with 0.1% v/v formic acid (B). A linear gradient from 20 to 35% B was applied for 6 minutes, followed by an equilibration step down to 20% B over 2 minutes. Mass spectrometric detection was performed with electrospray ionization in positive ion mode (ESI +) using MS scan mode (m/z range 400–1500). Cone and capillary voltages were set at 31 V and 3.2 kV, respectively; the source temperature was kept at 150°C with a desolvation temperature at 500°C and a gas flow of 800 L/hour. The LC/MS TIC chromatograms were displayed using MassLynx 4.1 (RRID:SCR_014271) to extract the spectrum with charge state distribution for each peak. Deconvolution was performed using ESIProt 1.1.

Tumor inhibition

Animal care and experiment were approved by the local Experimental Animal Ethics Committee of the BUC-CMMI (ref. CMMI-2019–01) and were conducted in compliance with the Belgian Royal

Decree of 29 May 2013 on the protection of laboratory animals. The antitumoral activity of Nanofitin-MMAE drug conjugates was assessed in an A431-Luc+ xenograft model. EGFR-positive A431 cells (RRID:CVCL_0037) were transduced to express a luciferase gene to monitor the tumor growth and indirectly assess cell viability, as described for the development of antiEGFR chimeric antigen receptor (CAR) expressing T cells (36).

Cells inoculation, treatment and tumor volume monitoring

Thirty-five 6-week-old BALB/c nude female mice (CAnN. Cg-Foxn1^{nu}/Crl, #194, Charles River, RRID:IMSR_CRL:194) were inoculated with 5×10^6 A431 luciferase-positive (A431-Luc+)-EGFR expressing cells in serum-free medium. Tumor volumes were measured three times a week with a caliper during the whole experiment. They were calculated as follows: Vtum $= 0.5\times L\times l^2$ with L = highest distance that is crossing the tumor and l = lowest distance that is crossing the tumor. When tumor volume reached 90 mm^3 size, intravenous injections of the Nanofitin-vc-MMAE conjugates (3 mg/kg mouse, 5 mice/group) were performed three times a week to reach a total of 12 injections per mouse, with at least one resting day between two injections. Five mice were also injected intravenously with 0.9% saline solution as controls (vehicle) following the same dosing schedule. Mice were sacrificed when tumor volumes reached 2,000 mm^3. Clinical signs and cohorts' survival were monitored till ten weeks after the first round of injection of Nanofitin-drug conjugates.

Tumor cell viability monitoring by bioluminescence imaging

Bioluminescence imaging (BLI) of the whole mice was performed twice a week to follow *in vivo* tumor growth and was expressed as the tumor growth percentage relative to day 3. Bioluminescence imaging was performed by means of a Photon Imager Optima (Biospace Lab) that dynamically counted the emitted photons for at least 25 minutes, under anesthesia (4% and 2% isoflurane for initiation and maintenance, respectively) and after subcutaneous administration of 150 mg/kg of D-luciferin (Promega). Image analysis was performed with M3Vision software (Biospace Lab). Regions of interest were drawn on the mice tumors, and signal intensities were quantified individually for a time lapse of 5 minutes corresponding to the maximum signal intensity plateau. Acceptance or rejection of a non-zero slope was statistically determined on the first 30 days corresponding to the period of treatment. The BLI data were analyzed by linear regression in GraphPad Prism 6 (GraphPad Inc, RRID:SCR_002798).

Anatomo-pathology analysis of tumor

Animal care and experiment were approved by the local Experimental Animal Ethics Committee of the BUC-CMMI (ref. CMMI-2013–05 and CMMI-2019–01) and were conducted in compliance with the Belgian Royal Decree of 29 May 2013 on the protection of laboratory animals. The intratumoral penetration of Nanofitins was assessed in an A431 xenograft model.

Cells inoculation, treatment, and tissue processing

Eight-week-old BALB/c nude female mice (CAnN.Cg-Foxn1^{nu}/Crl, #194, Charles River, RRID:IMSR_CRL:194) were inoculated with 5×10^6 A431 EGFR-expressing cells (RRID:CVCL_0037) in serum-free medium. Tumor volumes were measured and calculated as described previously. When tumor volume reached 150 mm^3 size, a single dose of HA-tagged Nanofitin (66 μg) or Cetuximab (1 mg, Erbitux, 217801, Merck) was injected intravenously (5 mice/group) to achieve the same molar dose. Mice were sacrificed 90 minutes post injection to harvest the flanked tumors. After tumor resection and standard formalin-fixed and paraffin-embedded (FFPE) tissue processing, serial tumor slices were subjected to IHC to evidence CD31 in addition to Cetuximab and/or Nanofitin.

IHC

Nanofitins were HA-tagged (35) for detection by IHC, whereas Cetuximab was detected by anti-human IgG. CD31/PECAM (Platelet Endothelial Cell Adhesion Molecule-1) were used to detect endothelial cells. Immunostainings were performed using Discovery XT (Ventana Medical Systems, Roche Diagnostics) and DABMap detection systems according to the manufacturer's recommendations. Four-micrometer-thick sections were deparaffinized and rehydrated. Heat-induced epitope retrieval was performed using Cell Conditioning Solution pH 8.4 during 36 minutes at 100°C. Next, slices were incubated with primary antibodies anti-CD31 (Cell Signaling, #77699, diluted 1:100, 2 hours, RRID:AB_2722705), anti-HA-tag (Cell Signaling, #3724, diluted 1:100, 1 hour, RRID:AB_1549585), or anti-human IgG (Abcam, #Ab109489, diluted 1:300, 1 hour, RRID:AB_10863040). Subsequently, slices were incubated with a Goat Anti-Rabbit IgG Antibody (H+L), Biotinylated secondary antibody (1:200, BA-1000, Vector Laboratories, RRID:AB_2313606). Sections were counterstained with hematoxylin and mounted with Entellan.

Whole-slide imaging and digital image analysis

The whole-slides were digitized at 20× (0.453 μm side pixel) using a Hamamatsu 2.0 HT scanner (Hamamatsu, RRID:SCR_021658), which was calibrated beforehand using a specific slide provided by the manufacturer. Whole-slide images were normalized using a methodology previously validated (37). Image processing and analysis were then performed as detailed elsewhere (38). Briefly, pairs of virtual slides targeting CD31 and the active compound to analyze (the Nanofitins or Cetuximab) were subjected to image registration. The CD31- and compound-positive cells were then automatically detected in the aligned virtual slides. In addition, up to 7 concentric tumor regions (27 μm-width each) were automatically delineated around the blood vessels identified by the CD31-positive staining (Supplementary Fig. S2), then transferred to the slide images showing the compounds. The percentages of positive cells were determined as labeling indexes for each compound in each concentric tumor region, and were statistically compared by one-way ANOVA in GraphPad Prism 6 (GraphPad Inc, RRID:SCR_002798).

Data availability statement

The data generated in this study are available upon request from the corresponding author.

Results

Nanofitins show fast and deep EGFR+ tumor targeting

IHC experiments on A431 xenograft tumors were performed to observe the Nanofitins accumulation within solid tumors with a maximal contrast (32), in comparison to the reference antibody Cetuximab (6). Individual positive-cells were detected for each compound, resulting in labeling indexes, obtained in up to seven concentric tumor regions delineated around the blood vessels (Supplementary Fig. S2).

As expected from a xenograft model, CD31 staining revealed endothelial cells from the host vasculature, infiltrated in each human tumor. Anti-IgG and anti-HA staining from consecutive slides allowed to localize Cetuximab or HA-tagged Nanofitins, respectively. From the same molar dose administered systemically, we report an extensive

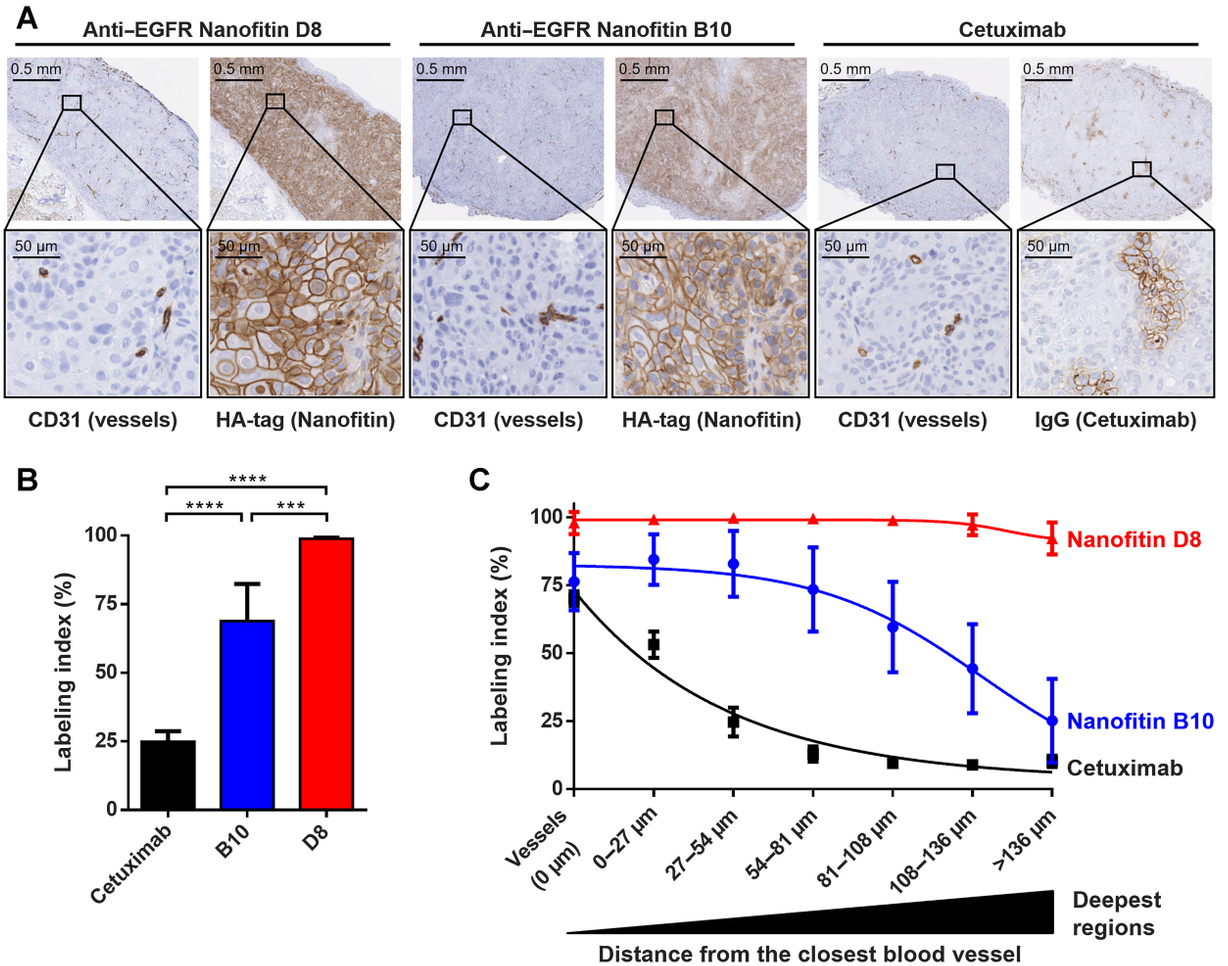

Figure 1.

Intratumoral infiltration 90 minutres after systemic administration. **A,** Intratumoral infiltration of antiEGFR Nanofitins or Cetuximab, revealed by anti-HA and anti-IgG IHC, respectively. Host vasculature is revealed by anti-CD31 staining of consecutive slice sections. Zoom of selected regions illustrates EGFR labeling at the vessel proximity. **B,** Labeling index, on the basis of cells positively labeled, in the whole tumor. **C,** Labeling index relative to the distance from the closest blood vessel. ****, $P < 0.0001$; ***, $P < 0.0005$.

tumor penetration 90 minutes postinjection with HA-tagged Nanofitin D8 (98.9% ± 0.7 cells labeled, $n = 5$; **Fig. 1**). Deep infiltration was also observed with HA-tagged Nanofitin B10 (67.9% ± 14.1, $n = 5$) as opposed to Cetuximab that appeared highly constrained (24.3% ± 4.1, $n = 4$). A larger SD was observed with B10 and was attributed to blood-tinged necrosis at the core of the tumors, which is commonly undergone by A431-based models. On the contrary, D8 variability is especially low due to near-complete tumor labeling, resulting in more than 92% of labeled cells beyond 136 µm from the vessels. In the same conditions, the Cetuximab labeling index is close to the B10 labeling index within the vessel regions of interest (0 µm) and stays significantly restrained to the vessel's proximity.

Regioselective assembly of Nanofitin-drug conjugates

Nanofitin-drug conjugates were generated by regioselective conjugation via maleimide chemistry on a C-terminal engineered-cysteine (**Fig. 2A**). Analysis by UPLC-RP/MS confirmed the conjugation of a single vc-MMAE payload per Nanofitin, with purity yields ranging from 97 to 100% on the 3 different Nanofitin-drug conjugates (**Fig 2B**), and undetected residual MMAE levels (under 0.4 ng/mL).

Binding characteristics of either the unconjugated Nanofitins or the Nanofitin-drug conjugates were evaluated on human EGFR by interferometry (**Fig. 2C** and **Table 1**). The Nanofitin D8 showed slower association and dissociation rates with single-digit nanomolar affinities before and after conjugation. Molecules derived from the Nanofitin B10 displayed faster on- and off-rates, as described previously with the parental unconjugated Nanofitin B10 (32). We noted an impact on B10 affinity upon conjugation with a K_D shifting from 27.6 nmol/L to 114.2 nmol/L. In addition, the antiEGFR Nanofitins D8 and B10 were demonstrated to bind human and mouse forms of EGFR (**Table 1**; Supplementary Fig. S3). The binding of D8 constructs to the human EGFR was marked with a 1-log slower off-rate, resulting in a 1-log difference of the overall equilibrium constants (K_D). While the kinetic profiles appeared similar between the two forms of EGFR, the binding of B10 to the human EGFR was marked with a slightly faster off-rate.

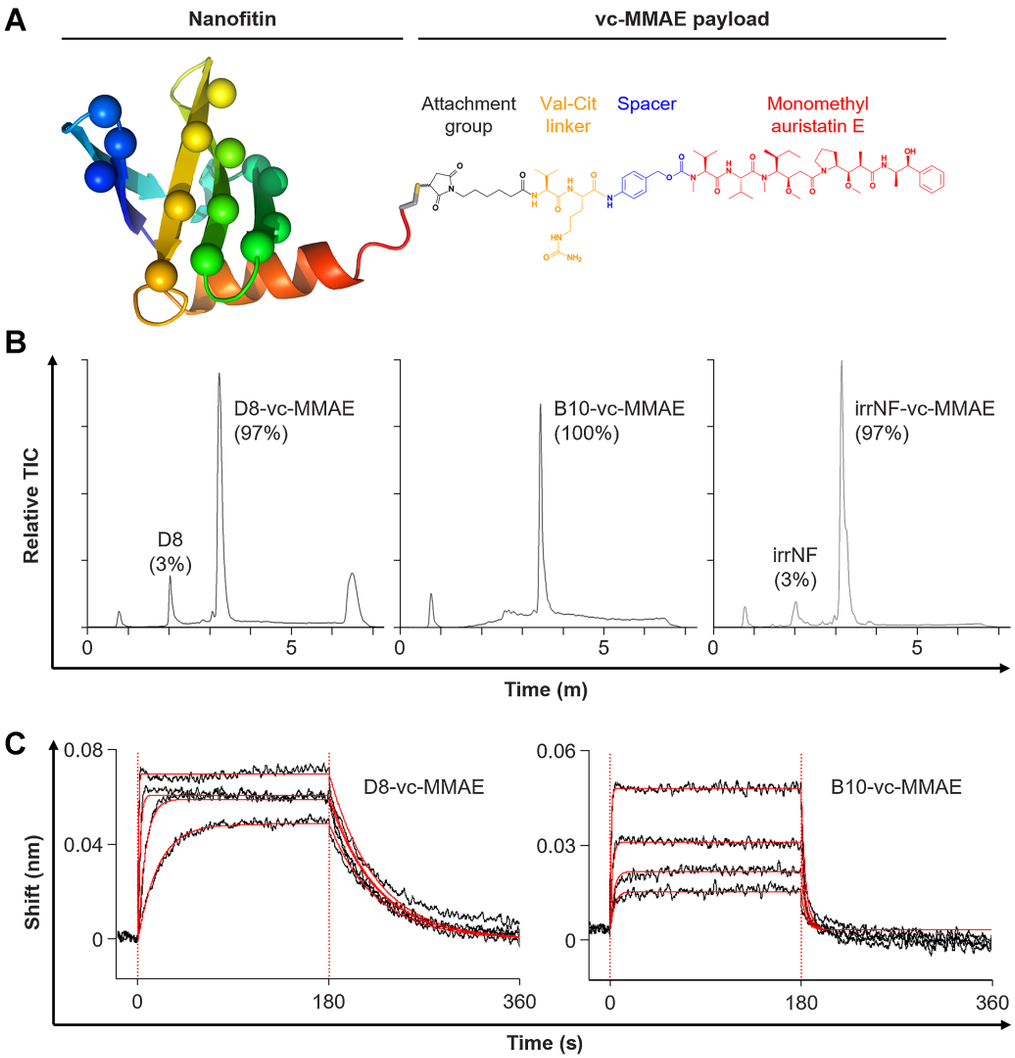

Figure 2.

Biochemical profiles of Nanofitin-drug conjugates. **A,** Schematic representation of a Nanofitin-drug conjugate. The single chain of the Nanofitin scaffold (rainbow cartoon) is engineered to target EGFR by randomizing up to 14 amino acids (spheres in lieu of carbon alpha). Each Nanofitin is genetically fused to a C-terminal cysteine (gray/yellow stick) to allow the regioselective chemistry on the only thiol group. The vc-MMAE payload (structural formula) is coupled via its maleimide-based moiety (black) and releases the MMAE toxin (red) after proteolytic cleavage of the valine-citrulline linker (orange). **B,** UPLC-RP/MS profiles. Peaks were identified by ESI-MS spectral deconvolution to determine their mass. Percentages of corresponding species were determined from the area under the absorbance curves. **C,** Determination of the binding characteristics of the antiEGFR Nanofitin-drug conjugates D8-vc-MMAE (left) and B10-vc-MMAE (right) by biolayer interferometry on human EGFR, using the antiEGFR Nanofitin at concentrations of 500, 125, 31.25, and 7.81 nmol/L. Fittings are represented as solid red lines.

Efficacy of D8-vc–MMAE in mice bearing A431-luc+ xenografts

Each Nanofitin-drug conjugate was administered intravenously three times a week, to reach a total of 12 injections, to mice bearing A431-Luc+ subcutaneous xenograft. To reduce the effect of the intrinsically heterogeneous growth of A431-Luc+ tumors, the first doses were injected once tumors reached a minimum of 90 mm^3, resulting in a mean initial volume of 155±77 mm^3. Mice treated with D8-vc–MMAE showed constant tumor volumes for 2 months, during both administration and follow-up periods (**Fig. 3A**). Groups treated with vehicle, irrNF-vc-MMAE or B10-vc-MMAE showed significant tumor growth and multiple mice reached humane endpoints before the last injection. Tumor growth was still heterogeneous within groups treated with vehicle, irrNF-vc–MMAE or B10-vc–MMAE. Such variability was considered as a mark of little inhibitory effect, whereas the group treated with D8-vc–MMAE presented low SD attributed to an efficient tumor inhibition during the treatment and the subsequent monitoring period.

Bioluminescence imaging (BLI) was performed for each animal to confirm the treatment efficacy. At the beginning of the study, normalized bioluminescence signals defined an initial baseline between 10^{10} and 10^{11} ph/s/cm^2/sr. Treatment with recurrent injections of D8-vc–MMAE triggered a significant drop in bioluminescence before the end of week 2, whereas vehicle, irrNF-vc-MMAE and B10-vc-MMAE showed little effect for the first 3 weeks. The statistical analysis of the luciferase activity during the treatment period demonstrated that only xenograft tumors

Table 1. Affinity determination against human and mouse EGFR.

	Human EGFR				Mouse EGFR			
	K_D (nM)	k_{on} (10^6 $M^{-1}.s^{-1}$)	k_{off} (10^{-2} s^{-1})	R^2	K_D (nM)	k_{on} (10^6 $M^{-1}.s^{-1}$)	k_{off} (10^{-2} s^{-1})	R^2
D8	5.56 ± 0.05	1.55 ± 0.01	0.86 ± 0.00	0.96	59.69 ± 3.01	1.74 ± 0.08	10.40 ± 0.16	0.94
D8-HA	5.29 ± 0.05	1.70 ± 0.02	0.90 ± 0.00	0.96	54.17 ± 2.61	1.77 ± 0.08	9.59 ± 0.14	0.94
D8-vc-MMAE	5.85 ± 0.08	3.88 ± 0.05	2.27 ± 0.01	0.99	N.D.	N.D.	N.D.	N.D.
B10[a]	27.6	1.90	5.24	0.99	83.0	1.41	11.7	0.98
B10-HA	48.80 ± 1.39	2.09 ± 0.06	10.18 ± 0.09	0.98	143.60 ± 5.92	2.68 ± 0.10	38.44 ± 0.53	0.99
B10-vc-MMAE	114.20 ± 6.40	2.03 ± 0.11	23.14 ± 0.39	0.98	N.D.	N.D.	N.D.	N.D.

Binding characteristics of the antiEGFR Nanofitins and Nanofitin-drug conjugates determined by biolayer interferometry on human and mouse EGFR. D8 and B10: Nanofitins without C-terminal tag. D8-HA and B10-HA: Nanofitins with a C-terminal HA-tag. D8-vc-MMAE and B10-vc-MMAE: Nanofitin-drug conjugates with a C-terminal payload.
[a]According to Goux, *et al* (32). N.D.: Not determined.

exposed to D8-vc–MMAE validated a nonzero slope hypothesis ($P < 0.0001$; **Fig. 3B**), indicating an elimination of EGFR+ tumor cells *in vivo*. Out of the four mice monitored after 50 days, three showed BLI signals equivalent to the background noise (10^3 ph/s/cm^2/sr) while the fourth mouse showed limited BLI signals (10^6 ph/s/cm^2/sr). Overall, survivors bearing tumors showed a 1-to-2 log drop of signal intensities during the second month, suggesting that the anti-tumor effect triggered by D8-vc-MMAE persists after clearance of the product. Each other molecule showed little anti-tumor effect with tumor growth inhibitions slower than with D8-vc–MMAE, if significant. We attributed drops in BLI signals after 1 month to metabolic fatigue or blood-tinged necrosis established at the core of the A431-Luc+ tumors.

Given the necrosis-prone nature of A431-derived tumor implants (also observed by IHC; **Fig. 2**), morphologic analysis of the tumors was conducted and confirmed the difference between D8-vc–MMAE treated mice and other animals. Efficient tumor growth inhibition was supported by reshaped, opacified and hardened yellowish tumors over time with D8-vc–MMAE. In contrast, active tumors in other groups tended to be softer, showed necrotic cavities at their core and were more active on their periphery.

The safety of the approach was evaluated by monitoring the body weight of each animal during the first 25 days of treatment (**Fig. 4**). Only one mouse, in the B10-vc-MMAE group, was sacrificed due to body loss combined with advanced necrosis (circle). Each other animal showed constant or increasing body weight over time. Three animals in

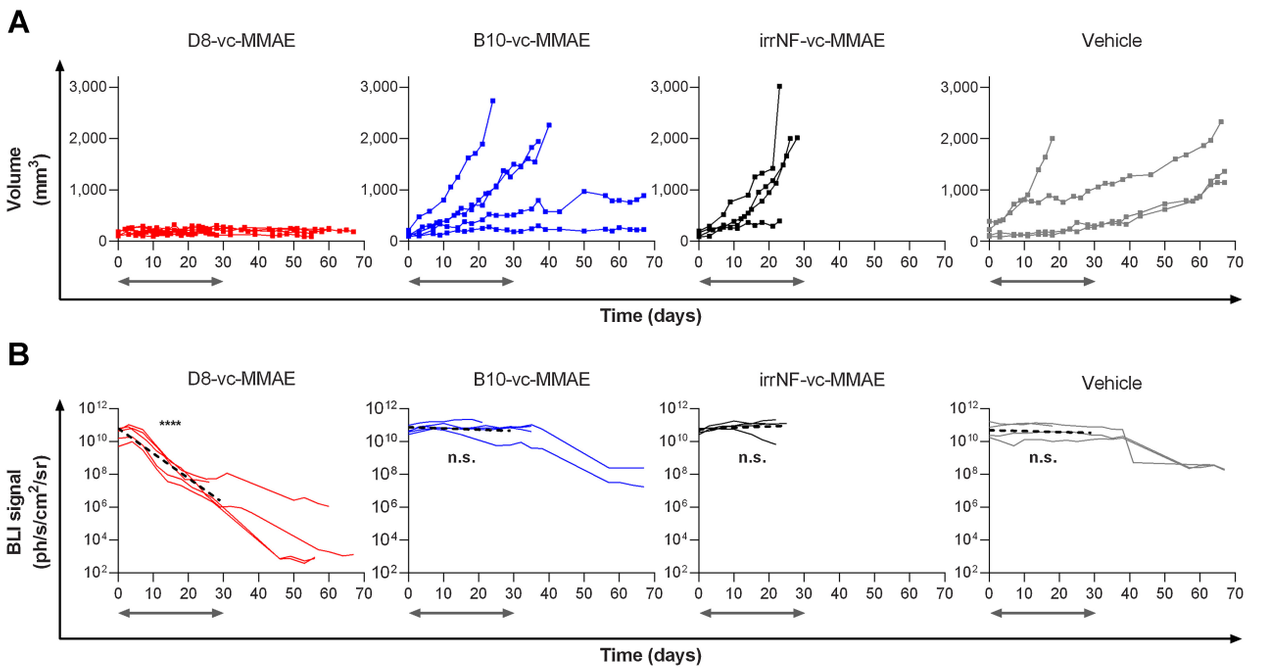

Figure 3.
Therapeutic efficacy of D8-vc-MMAE against A431-Luc+ tumor xenograft model in nude mice. Mice were treated with 3 mg/kg of Nanofitin-drug conjugates or vehicle. Time zero of the treatment is set when tumor volume reaches 90 mm^3. Gray arrows indicate the period of treatment. **A,** Individual tumor growing curves. **B,** Individual bioluminescence imaging curves (solid) and simple linear regression curve during treatment (dashed) statistically compared to a nonzero slope hypothesis. ****, $P < 0.0001$; n.s.: not significant.

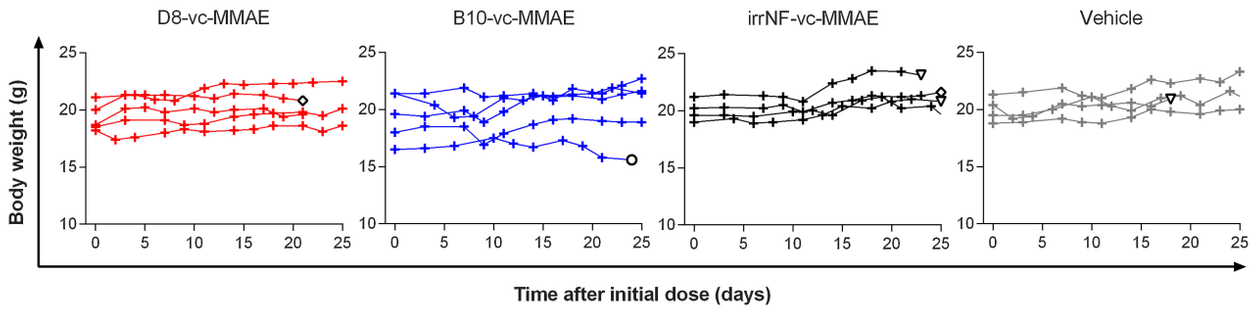

Figure 4.
Body weight monitoring during the first 25 days of treatment. White symbol with black outline: mouse sacrificed because of torn out tumor (diamond), advanced necrosis (triangle) or body-weight loss and necrosis (circle).

the irrNF-vc-MMAE and vehicle groups reached humane endpoints and were sacrificed because of the advanced necrosis of their tumor, representative of little inhibitory effect of the treatment. Finally, one animal in the irrNF-vc-MMAE group and the only sacrificed animal in the D8-vc-MMAE group during the treatment period tore out their xenograft and were subsequently sacrificed.

Discussion

The ultimate goal of anti-tumor therapies is to selectively target and kill all the tumor cells while sparing healthy tissues. Conceptually, ADCs meet these requirements with the selectivity of an antibody and the cytotoxic potency of its payload. Despite a growing interest in the technology and a still increasing number of ADC in clinical trials (10), the attrition rate remains high and mainly driven by a lack of efficacy and safety concerns. Some of the limitations of ADCs are inherently associated with the pharmacokinetic and physicochemical properties of full-length antibodies such as hepatic clearance, a slow tumor uptake, avidity via their two binding sites and a long plasma half-life.

In this study, we evaluated the fitness of the small Nanofitin scaffold for the generation of drug conjugates, using the clinically validated protease-labile valine-citrulline linker and the auristatin derivative MMAE as a cytotoxic payload (**Fig. 2A**). Tumor targeting was achieved using antiEGFR Nanofitins (32) D8 and B10, which compete with Cetuximab (Supplementary Fig. S4), cross-react with both human and murine EGFR, and have similar affinity constants (K_D of 5.56 and 27.6 nmol/L respectively; **Table 1**). These affinities fall in the range described for selective EGFR+ tumors targeting over healthy EGFR-expressing tissues (39). We observed that while targeting an overlapping epitope (Supplementary Fig. S4), the two Nanofitin ligands differ from Cetuximab (40) in their ability to cross-react with mouse EGFR. Such cross-reactivity, beneficial for therapeutic development to demonstrate the absence of adverse effects, may be attributed to their *in vitro* selection process (27–34) that is not restricted by immunization determinism. The antiEGFR Nanofitin D8, initially referred as αEGFR_NF2, was internalized after incubation with A431 carcinoma cells (32). In similar conditions, no meaningful internalization of B10 could be observed, indicating that these two Nanofitins exhibit a different ability at inducing receptor-mediated endocytosis.

The two HA-tagged Nanofitins, able to engage the cell surface receptor (Supplementary Fig. S5), displayed a broad intratumoral infiltration 90 minutes after their tail-vein injection in an A431 tumor xenograft murine model, as shown by IHC (**Fig. 1**). IHC results revealed an engagement of 67.9% ± 14.1 and 98.9% ± 0.7 of the tumor cells, respectively for B10 and D8. The penetration of D8 was highly homogeneous within all of the tumor, while the level of cells labelled by B10 appeared to decrease down from 75% starting from up to 80 µm away from the closest vessel to 25% in the deepest regions (136+ µm). Further evaluations would be required to decipher whether their differential accumulation level is linked to their different dissociation rates (0.90×10^{-2} s^{-1} for D8-HA and 10.18×10^{-2} s^{-1} for B10-HA) or other physicochemical properties (e.g.,: internalization, charge). This IHC dataset highlights the faster penetration potential of the antiEGFR Nanofitins as compared with the antibody Cetuximab at this time point. In our study, only 24.3% ± 4.1 of the tumor cells were labelled by Cetuximab, which was found mainly restricted within the perivascular space in an area of up to 27 µm from the vasculature. Our results are in agreement with the finding of Lee and Tannock, who also reported a staining of Cetuximab mainly in the perivascular space of A431 xenografts with the same injected dose (1 mg; ref. 6). The binding site barrier has been reported to slow down the diffusion rate of Cetuximab (6) in the high EGFR-expressing tumors A431 ($2–3\times10^6$ EGFR molecules per cell), with higher avidity in a context of high target density. The monovalent-binding kinetic profiles of the antiEGFR Nanofitins could also contribute to their faster diffusion in this tumor xenograft model as compared with that of the bivalent antibody Cetuximab. In another study comparing several drug conjugate formats, Nessler and colleagues also reported that a monovalent format could result in a better antitumor efficacy due to a higher penetration and an increased number of cells exposed to lethal payload doses (41). It remains to be investigated whether the binding kinetics of the antiEGFR Nanofitins also support high accumulation in other tumors expressing a lower level of the tumor antigen. Alternatively, both affinity (30) and valence of Nanofitins can be tuned using straightforward protein engineering strategies.

Nanofitin-vc–MMAE drug conjugates were generated by engineering the Nanofitins to exhibit a single and solvent accessible cysteine. It enables thiol-based regioselective conjugation with the maleimide activated MMAE toxin, leading to highly homogeneous conjugates with overall purity of ≥ 97% (**Fig. 2B**). Despite the high tumor accumulation observed for both D8 and B10 Nanofitins, only D8-vc–MMAE compound yielded high antitumor activity compared with the controls treated with the vehicle only or with a nontargeting drug conjugate based on a Nanofitin that binds specifically to hen-egg white lysozyme [irrNF, irrelevant Nanofitin (refs. 42, 43)]. The activity of D8-vc-MMAE was confirmed by both a strong inhibition of the tumor growth as well as reduction of the luciferase activity, hence the cell viability, within the residual tumor tissue (**Fig. 3**). The differential antitumoral effect between D8- and B10-vc-MMAE drug conjugates

suggests that efficient tumor targeting, inferred from IHC with HA-tagged Nanofitins derived from D8 and B10, is not sufficient for a therapeutic activity. Bennett and colleagues compared the antitumor efficacy of MMAE and MMAF cytotoxic payload targeted with a bicycle peptide (44). Greater tumor growth inhibition was observed with the MMAE-based drug conjugate. The difference of activity was attributed to the bystander activity of MMAE that is absent with MMAF. However, whether internalization was required for the activation of the toxin, or could result from its extracellular cleavage in the tumor microenvironment, remained elusive and the authors concluded that it is likely that it results from a combination of both. Although we cannot rule out the possibility that the toxin was activated extracellularly in our study, the lack of antitumor activity observed with the noninternalizing B10-MMAE drug conjugate suggests that the internalization may be required for therapeutically relevant toxin release in the preclinical model that we used. Interestingly, monitoring of mice over 2 months showed that D8-vc-MMAE prevented recurrence of the tumor, as demonstrated by morphologic analysis and bioluminescence imaging, suggesting that the efficient tumor penetration of the drug could give rise to complete remission. Aside from its high antitumor activity, i.e., its high local cytotoxicity, we observed no sign of systemic toxicity upon D8-vc-MMAE administration, as evidenced by the constant body weights during treatment (**Fig. 4**). We anticipate that such a behavior *in vivo* is encouraging for future toxicity studies, as the Nanofitin D8 is able to bind to EGFR not only from the xenograft but also from the host, whilst we acknowledge a 1-log affinity difference for the two receptors (**Table 1**). To maximize exposure, dosing schedule of the Nanofitin-drug conjugates consisted in three intravenous injections a week, up to a total of 12 injections. It would be interesting to evaluate the duration of tumor exposure to cytotoxic dose of the payload upon a bolus administration of the Nanofitin-drug conjugate to rationalize the administration scheme. A sustained tumor exposure to the toxin, supporting a weekly dosing, was reported with a single-bolus injection of bicycle peptide-MMAE conjugate (44). Reducing the administration frequency of the Nanofitin-vc-MMAE drug conjugate shall foster the translatability of this approach into clinical setting.

In conclusion, we demonstrated with this study that the Nanofitin technology exhibits the attributes for an efficient and safe tumor targeting of potent cytotoxic payloads like the auristatin derivative MMAE. Owing to its small molecular size and monovalent format, the antiEGFR Nanofitin-drug conjugate D8-vc-MMAE penetrated deeply within A431 tumor tissue, yielding to a targeting of nearly all of the tumor cells. Its ability at triggering receptor-mediated endocytosis may play a critical role in facilitating the efficient release of the MMAE toxin and subsequent antitumor effect. In addition, the rapid clearance of Nanofitins by renal filtration provides the potential to overcome one of the current safety concerns with ADCs.

Authors' Disclosures

S. Huet reports grants from European Commission and personal fees from Affilogic during the conduct of the study; and commercialization by Affilogic of the Nanofitin technology described in the study. R. Castro reports grants from Agência Nacional de Inovação for Portugal (E!11391 ONCOFITIN) during the conduct of the study. P. Jacquot reports grants from European Commission and personal fees from Affilogic during the conduct of the study; and commercialization by Affilogic of the Nanofitin technology described in the study. J. Pedrault reports grants from European Commission and personal fees from Affilogic during the conduct of the study; and commercialization by Affilogic of the Nanofitin technology described in the study. S. Viollet reports grants from European Commission and personal fees from Affilogic during the conduct of the study; and commercialization by Affilogic of the Nanofitin technology described in the study. G. Doumont reports grants from ULB-CMMI and other support from Affilogic during the conduct of the study. A.E. Cunha reports grants from Agencia Nacional de Inovacao for Portugal (E!11391 ONCOFITIN) during the conduct of the study. M. Cinier reports grants from European commission and personal fees from Affilogic during the conduct of the study; and commercialization by Affilogic of the Nanofitin technology described in the study. No disclosures were reported by the other authors.

Authors' Contributions

S. Huet: Conceptualization, resources, data curation, formal analysis, supervision, validation, investigation, visualization, methodology, writing–original draft, writing–review and editing. **M. Zeisser Labouebe:** Conceptualization, resources, formal analysis, investigation, visualization, methodology, writing–review and editing. **R. Castro:** Conceptualization, resources, validation, investigation, methodology, writing–review and editing. **P. Jacquot:** Validation, investigation. **J. Pedrault:** Validation, investigation. **S. Viollet:** Resources, validation, investigation, visualization, methodology, writing–review and editing. **G. Van Simaeys:** Data curation, validation, investigation, visualization, methodology. **G. Doumont:** Resources, investigation, methodology. **L. Larbanoix:** Resources, formal analysis, investigation, visualization, methodology. **E. Zindy:** Resources, software, formal analysis, investigation, visualization, methodology. **A.E. Cunha:** Supervision, funding acquisition, investigation. **L. Scapozza:** Conceptualization, funding acquisition, writing–review and editing. **M. Cinier:** Conceptualization, funding acquisition, writing–original draft, writing–review and editing.

Acknowledgments

This project was partially sponsored from November 2017 to February 2020 by a grant from Eurostars / the European Commission via Banque Publique d'Investissement for France (DOS0059903), the Agência Nacional de Inovação for Portugal (E!11391 ONCOFITIN) and Innosuisse for Switzerland (1315001273). CMMI is supported by the European Regional Development Fund and the Walloon Region. GVS and GD are also supported by the Fondation ULB, the Fonds Erasme and "Association Vinçotte Nuclear" (AVN). We are grateful to Justine Picot, Anaëlle Perrocheau, Harmony Gorré, Chloé Savignard, Anne Chevrel, Léo Candela, Caroline Roze, Rémi Gaillard, Elise Enouf and Maurine Fleury from Affilogic for their involvement and technical support. We acknowledge Sónia Mendes, Rute P. Eleutério, Mónica Thomaz and Filipe Pinto for their technical support on the project at iBET. We thank the Center for Microscopy and Molecular Imaging (CMMI) for their contribution to the experiments with the xenograft model, especially Cedric Balsat, Justine Allard, Yves-Rémy Van Eycke, Coraline De Maeseneire, Nicolas Passon, Isabelle Salmon and Christine Decaestecker.

The publication costs of this article were defrayed in part by the payment of publication fees. Therefore, and solely to indicate this fact, this article is hereby marked "advertisement" in accordance with 18 USC section 1734.

Note

Supplementary data for this article are available at Molecular Cancer Therapeutics Online (http://mct.aacrjournals.org/).

Received December 16, 2022; revised April 13, 2023; accepted August 10, 2023; published first August 14, 2023.

References

1. Mancini SJC, Balabanian K, Corre I, Gavard J, Lazennec G, Bousse-Kerdilès M-CL, et al. Deciphering tumor niches: lessons from solid and hematological malignancies. Front Immunol 2021;12:766275.
2. Dreher MR, Liu W, Michelich CR, Dewhirst MW, Yuan F, Chilkoti A. Tumor vascular permeability, accumulation, and penetration of macromolecular drug carriers. JNCI J Natl Cancer Inst 2006;98:335–44.
3. Tsuchikama K, An Z. Antibody-drug conjugates: recent advances in conjugation and linker chemistries. Protein Cell 2018;9:33–46.
4. Ponziani S, Di Vittorio G, Pitari G, Cimini AM, Ardini M, Gentile R, et al. Antibody-drug conjugates: The new frontier of chemotherapy. Int J Mol Sci 2020;21:1–28.
5. Zhao J. Cancer stem cells and chemoresistance: The smartest survives the raid. Pharmacol Ther 2016;160:145–58.

6. Lee CM, Tannock IF. The distribution of the therapeutic monoclonal antibodies cetuximab and trastuzumab within solid tumors. BMC Cancer 2010;10:255.
7. Xenaki KT, Oliveira S, van Bergen en Henegouwen PMP. Antibody or antibody fragments: Implications for molecular imaging and targeted therapy of solid tumors. Front Immunol 2017;8:1287.
8. Juweid M, Neumann R, Paik C, Perez-Bacete MJ, Sato J, van Osdol W, et al. Micropharmacology of monoclonal antibodies in solid tumors: direct experimental evidence for a binding site barrier. Cancer Res 1992;52:5144–53.
9. Labani-Motlagh A, Ashja-Mahdavi M, Loskog A. The tumor microenvironment: a milieu hindering and obstructing antitumor immune responses. Front Immunol 2020;11:1–22.
10. Dean AQ, Luo S, Twomey JD, Zhang B. Targeting cancer with antibody-drug conjugates: Promises and challenges. MAbs 2021; 13:1951427.
11. Vasalou C, Helmlinger G, Gomes B. A mechanistic tumor penetration model to guide antibody drug conjugate design. PLoS One 2015;10:1–20.
12. Joubert N, Beck A, Dumontet C, Denevault-Sabourin C. Antibody–drug conjugates: The last decade. Pharmaceuticals 2020;13:1–30.
13. Esnault C, Schrama D, Houben R, Guyétant S, Desgranges A, Martin C, et al. Antibody–drug conjugates as an emerging therapy in oncodermatology. Cancers (Basel) 2022;14:778.
14. Eigenmann MJ, Fronton L, Grimm HP, Otteneder MB, Krippendorff BF. Quantification of IgG monoclonal antibody clearance in tissues. MAbs 2017; 9:1007–15.
15. Mckertish CM, Kayser V. Advances and limitations of antibody drug conjugates for cancer. Biomedicines 2021;9:872.
16. Hoffmann RM, Coumbe BGT, Josephs DH, Mele S, Ilieva KM, Cheung A, et al. Antibody structure and engineering considerations for the design and function of antibody drug conjugates (ADCs). Oncoimmunology 2018;7:e1395127.
17. Orcutt KD, Adams GP, Wu AM, Silva MD, Harwell C, Hoppin J, et al. Molecular simulation of receptor occupancy and tumor penetration of an antibody and smaller scaffolds: application to molecular imaging. Mol Imaging Biol 2017;19: 656–64.
18. Schmidt MM, Wittrup KD. A modeling analysis of the effects of molecular size and binding affinity on tumor targeting. Mol Cancer Ther 2009;8:2861–71.
19. Srinivasarao M, Galliford CV, Low PS. Principles in the design of ligand-targeted cancer therapeutics and imaging agents. Nat Rev Drug Discov 2015;14:203–19.
20. Cazzamalli S, Dal Corso A, Widmayer F, Neri D. Chemically defined antibody- and small molecule-drug conjugates for in vivo tumor targeting applications: A comparative analysis. J Am Chem Soc 2018;140:1617–21.
21. Li Z, Krippendorff BF, Sharma S, Walz AC, Lavé T, Shah DK. Influence of molecular size on tissue distribution of antibody fragments. MAbs 2016;8:113–9.
22. Li Z, Li Y, Chang HP, Chang HY, Guo L, Shah DK. Effect of size on solid tumor disposition of protein therapeutics. Drug Metab Dispos 2019;47:1136–45.
23. Bennett G, Brown A, Mudd G, Huxley P, van Rietschoten K, Pavan S, et al. MMAE delivery using the bicycle toxin conjugate BT5528. Mol Cancer Ther 2020;19:1385–94.
24. ClinicalTrials.gov, Identifier NCT03486730, BT1718 in Patients With Advanced Solid Tumours (2018 Apr 3 -). Natl Libr Med 2000. Available at https://clinicaltrials.gov/ct2/show/NCT03486730.
25. ClinicalTrials.gov, Identifier NCT04180371, Study BT5528–100 in Patients With Advanced Solid Tumors Associated With EphA2 Expression (2019 Nov 27 -). Natl Libr Med 2000. Available at https://clinicaltrials.gov/ct2/show/NCT04180371.
26. Škrlec K, Štrukelj B, Berlec A. Non-immunoglobulin scaffolds: a focus on their targets. Trends Biotechnol 2015;33:408-18.
27. Béhar G, Bellinzoni M, Maillasson M, Paillard-Laurance L, Alzari PM, He X, et al. Tolerance of the archaeal Sac7d scaffold protein to alternative library designs: characterization of anti-immunoglobulin G Affitins. Protein Eng Des Sel 2013; 26:267–75.
28. Huet S, Gorre H, Perrocheau A, Picot J, Cinier M. Use of the Nanofitin alternative scaffold as a GFP-ready fusion tag. 2015;10:e0142304.
29. Chevrel A, Candela L, Innocenti E, Golibrzuch C, Skudas R, Schwämmle A, et al. Development of versatile affinity-based system for one step purification process: case of group a streptococcus vaccine. Biotechnol Bioeng 2022;119:3210-3220.
30. Garlich J, Cinier M, Chevrel A, Perrocheau A, Eyerman DJ, Orme M, et al. Discovery of APL-1030, a novel, high-affinity nanofitin inhibitor of C3-mediated complement activation. Biomolecules 2022;12:432.
31. Michot N, Guyochin A, Cinier M, Savignard C, Kitten O, Pascual M-H, et al. Albumin binding Nanofitins, a new scaffold to extend half-life of biologics – a case study with exenatide peptide. Peptides 2022;152:170760.
32. Goux M, Becker G, Gorré H, Dammicco S, Desselle A, Egrise D, et al. Nanofitin as a new molecular-imaging agent for the diagnosis of epidermal growth factor receptor over-expressing tumors. Bioconjug Chem 2017;28:2361–71.
33. Kalichuk V, Renodon-Corniere A, Behar G, Carrion F, Obal G, Maillasson M, et al. A novel, smaller scaffold for Affitins: Showcase with binders specific for EpCAM. Biotechnol Bioeng 2018;115:290-299.
34. Marcion G, Hermetet F, Neiers F, Uyanik B, Dondaine L, Dias AMM, et al. Nanofitins targeting heat shock protein 110: An innovative immunotherapeutic modality in cancer. Int J Cancer 2021;148:3019–31.
35. Field J, Nikawa J, Broek D, MAcDONALD B, lt Rodgers L, Wilson IA, et al. Purification of a RAS-responsive adenylyl cyclase complex from saccharomyces cerevisiae by use of an epitope addition method downloaded from. 1988. Available at http://mcb.asm.org/.
36. Albert S, Arndt C, Feldmann A, Bergmann R, Bachmann D, Koristka S, et al. A novel nanobody-based target module for retargeting of T lymphocytes to EGFR-expressing cancer cells via the modular UniCAR platform. Oncoimmunology 2017; 6:e1287246.
37. Van Eycke YR, Allard J, Salmon I, Debeir O, Decaestecker C. Image processing in digital pathology: An opportunity to solve inter-batch variability of immunohistochemical staining. Sci Rep 2017;7:1–15.
38. Godin L, Balsat C, Van Eycke YR, Allard J, Royer C, Remmelink M, et al. A novel approach for quantifying cancer cells showing hybrid epithelial/mesenchymal states in large series of tissue samples: Towards a new prognostic marker. Cancers (Basel) 2020;12:906.
39. Crombet T, Osorio M, Cruz T, Roca C, Del Castillo R, Mon R, et al. Use of the humanized anti-epidermal growth factor receptor monoclonal antibody h-R3 in combination with radiotherapy in the treatment of locally advanced head and neck cancer patients. J Clin Oncol 2004;22:1646–54.
40. Hoeben BAW, Molkenboer-Kuenen JDM, Oyen WJG, Peeters WJM, Kaanders JHAM, Bussink J, et al. Radiolabeled cetuximab: Dose optimization for epidermal growth factor receptor imaging in a head-and-neck squamous cell carcinoma model. Int J Cancer 2011;129:870–8.
41. Nessler I, Khera E, Vance S, Kopp A, Qiu Q, Keating TA, et al. Increased tumor penetration of single-domain antibody–drug conjugates improves in vivo efficacy in prostate cancer models. Cancer Res 2020;80:1268–78.
42. Cinier M, Petit M, Williams MN, Fabre RM, Pecorari F, Talham DR, et al. Bisphosphonate adaptors for specific protein binding on zirconium phosphonate-based microarrays. Bioconjug Chem 2009;20:2270–7.
43. Correa A, Pacheco S, Mechaly AE, Obal G, Bé Har G, Mouratou B, et al. Potent and specific inhibition of glycosidases by small artificial binding proteins (Affitins). PLoS One 2014;9:e97438.
44. Deonarain MP, Xue Q. Tackling solid tumour therapy with small-format drug conjugates. Antib Ther 2020;3:237–45.